Geophysical Journal International

Geophys. J. Int. (2024) **237,** 525–539
Advance Access publication 2024 February 08
GJI Applied and Marine Geophysics

https://doi.org/10.1093/gji/ggae050

Novel techniques for *in situ* estimation of shear-wave velocity and damping ratio through MASW testing part II: a Monte Carlo algorithm for the joint inversion of phase velocity and phase attenuation

Mauro Aimar [1], Sebastiano Foti[1] and Brady R. Cox[2]

[1] *Department of Structural, Building and Geotechnical Engineering (DISEG), Politecnico di Torino, Corso Duca degli Abruzzi* 24, 10129 *Torino, Italy.*
E-mail: mauro.aimar@polito.it
[2] *Department of Civil and Environmental Engineering, Utah State University,* 4110 *Old Main Hill, Logan, UT* 84321, *USA*

Accepted 2024 February 6. Received 2024 January 10; in original form 2023 March 24

SUMMARY

This paper deals with *in situ* characterization of the small-strain shear-wave velocity V_S and damping ratio D_S from an advanced interpretation of Multi-channel Analysis of Surface Waves (MASW) surveys. A new approach based on extracting Rayleigh wave data using the CFDBFa method has been discussed in the companion paper. This paper focuses on mapping the experimental Rayleigh wave phase velocity and attenuation into profiles of V_S and D_S versus depth, which is achieved through a joint inversion procedure. The joint inversion of phase velocity and attenuation data utilizes a newly developed Monte Carlo global search algorithm, which implements a smart sampling procedure. This scheme exploits the scaling properties of the solution of the Rayleigh eigenvalue problem to modify the trial earth models and improve the matching with the experimental data. Thus, a reliable result can be achieved with a limited number of trial ground models. The proposed algorithm is applied to the inversion of synthetic data and of experimental data collected at the Garner Valley Downhole Array site, as described in the companion paper. In general, inverted soil models exhibit well-defined V_S profiles, whereas D_S profiles are affected by larger uncertainties. Greater uncertainty in the inverted D_S profiles is a direct result of higher variability in the experimental attenuation data, the limited wavelength range at which reliable values of attenuation parameters can be retrieved, and the sensitivity of attenuation data to both D_S and V_S. Nonetheless, the resulting inverted earth models agree well with alternative *in situ* estimates and geological data. The results stress the feasibility of retrieving both stiffness and attenuation parameters from active-source MASW testing and the effectiveness of extracting *in situ* damping ratio estimates from surface wave data.

Key words: Elasticity and anelasticity; Inverse theory; Wave propagation.

1 INTRODUCTION

A reliable estimate of the small-strain shear-wave velocity V_S and damping ratio D_S is necessary for various applications in geotechnical earthquake engineering (for instance, ground motion amplification studies or the modelling of ground-borne vibrations), due to their relevant role in the stress-strain response of soils under dynamic loading. A possibility to obtain *in situ* estimates of V_S and D_S relies on the Multichannel Analysis of Surface Waves (MASW; Foti 2000). This procedure measures the spatial phase lag and attenuation of Rayleigh waves (or *R*-waves) along linear arrays with active sources. These experimental data are interpreted to retrieve the so-called dispersion curves and attenuation curves, hereafter labelled as $V_R(\omega)$ and $\alpha_R(\omega)$, that describe the frequency dependence of the *R*-wave phase velocity V_R (i.e. the propagation speed) and of the phase attenuation α_R (i.e. the spatial amplitude decay). Then, the V_S and the D_S profiles with depth are estimated through an inversion scheme, where a theoretical soil model is calibrated to match the experimental $V_R(\omega)$ and $\alpha_R(\omega)$. This paper focuses on new developments related to the joint inversion of experimental dispersion and attenuation data in order to retrieve estimates of the V_S and D_S profiles. New procedures for estimating the experimental dispersion and attenuation data are addressed in the companion paper (Aimar *et al.* 2024; hereafter labelled as 'Part I').

Inversion is a crucial step in MASW processing, as it maps experimental *R*-wave parameters into a suite of subsurface models.

However, the solution of the inverse problem is a mathematically complex operation, as it is a non-linear, mixed-determined, and ill-posed problem (e.g. Foti *et al.* 2014). The ill-posedness is responsible for the solution non-uniqueness, namely different ground models may provide a compatible degree of fit with the experimental data. For this reason, uncertainty bounds on the best solution should be included, or a set of equivalent solutions should be provided (Foti *et al.* 2018).

Furthermore, the highly non-linear nature of the optimization procedure urges to adopt specialized algorithms to ensure that the identified solution is the optimal one. In general, the most popular methods aiming at identifying the optimum can be clustered into two families: local search methods and global search methods. Local search methods are iterative, deterministic techniques that gradually adjust an initially assumed ground model to match the experimental data (e.g. Constable *et al.* 1987; Lai & Rix 1998; Xia *et al.* 1999; Badsar 2012; Verachtert *et al.* 2017). However, these schemes are strongly sensitive to the choice of the initial model (Spang 1995; Lai & Rix 1998). Global search methods are stochastic techniques that explore the model parameter space to identify the best model. These approaches generate random ground models, according to an assigned probability distribution, and the corresponding synthetic data are compared with the experimental ones. In many procedures, the sampling of the parameter space is optimized and iteratively refined over promising regions, limiting the required number of samples, and enhancing the quality of the final estimate (e.g. Sen & Stoffa 1996; Martı´nez *et al.* 2000; Wathelet *et al.* 2004; Socco & Boiero 2008). In general, global search methods are preferred over local search methods, as they do not require the definition of a first tentative profile. Besides, they allow the investigation of the uncertainties due to solution non-uniqueness. On the other hand, they are usually more time-consuming and computationally intensive (Foti *et al.* 2018). In some cases, a mixed inversion scheme is adopted. For instance, the Monte Carlo procedure can be used to estimate the uncertainties of the solution provided by a local estimator (Misbah & Strobbia 2014).

This paper proposes a new algorithm for the joint inversion of dispersion and attenuation data that relies on an improved Monte Carlo global search algorithm. In this approach, the optimization is achieved by exploiting the scaling properties of the Rayleigh eigenvalue problem in linear viscoelastic media, which are demonstrated herein. Therefore, the procedure represents a generalization of the algorithm introduced by Socco & Boiero (2008), for a viscoelastic model.

The paper starts with a general description of the inversion problem, to introduce basic notions and relevant terminology. Then, it describes the scaling properties of the Rayleigh eigenvalue problem, which represent the key feature in the proposed algorithm. Finally, the main steps of the inversion algorithm are summarized. The description includes an application of the proposed scheme to two synthetic examples and to site characterization of the Garner Valley Downhole Array site, whose phase velocity and attenuation data were estimated in Part I. The paper concludes with a discussion of the reliability of the derived S-wave velocity and damping ratio models.

2 THE INVERSION PROBLEM

The inversion relies on a physically-based model-data relationship, that can be described through the following general equation:

$$\mathbf{d} = \mathbf{g}(\mathbf{m}), \tag{1}$$

where $\mathbf{d}$ is the vector of measured data, $\mathbf{m}$ is the vector of the desired model parameters and $\mathbf{g}$ is a function relating these quantities. The latter provides an estimate of observed data when the model parameters are known, hence it is mathematically a forward problem (Tarantola 2004).

In surface wave testing aimed at jointly estimating stiffness and dissipation parameters of the soil deposit, $\mathbf{d}$ is the collection of experimental modal phase velocity $V_R(\omega)$ and phase attenuation $\alpha_R(\omega)$ data, whereas $\mathbf{m}$ is the set of parameters describing the geometry and the mechanical behaviour of the soil deposit. Usual inversion procedures model the soil deposit as a vertical stack of homogeneous and isotropic linear viscous elastic layers (Foti *et al.* 2018). Therefore, the unknown parameters are the number of layers and, for each layer, the thickness H (excluding the half-space), the mass density ρ, the S-wave velocity V_S, the P-wave velocity V_P (or, alternatively, the Poisson ratio ν), the S-wave damping ratio D_S, and the P-wave damping ratio D_P. The derivation of a subsurface model from experimental data relies on the frequency-dependence of R-wave propagation parameters $V_R(\omega)$ and $\alpha_R(\omega)$. This dependence is a combined effect of geometric dispersion, which results from the variation of mechanical properties with depth, and intrinsic dispersion, due to the constitutive behaviour of linear viscoelastic media (e.g. Shibuya *et al.* 1995; Foti *et al.* 2014). This relationship is synthesized by the Rayleigh wave eigenvalue problem, which maps the subsoil profile into the dispersive behaviour of the R-waves, hence it represents a forward relationship (i.e. the function $\mathbf{g}$). As the existence of the inverse function $\mathbf{g}^{-1}$ has not been demonstrated yet, the model identification is tackled through inversion theory, in which model parameters are calibrated so that the simulated system response (obtained by applying the forward problem in eq. 1) fits the experimental data. The degree of fit between the theoretical and experimental data is quantitatively measured by a misfit function, the minimization of which represents the goal of the inversion process.

A popular scheme for solving the inversion problem is the Monte Carlo sampling procedure, which is a family of global search algorithms that falls within the framework of Bayesian approaches. The aim of a Bayesian approach is the derivation of a posterior probabilistic distribution $\sigma(\mathbf{m})$ for a generic model $\mathbf{m}$, that statistically measures the ability of the model to be compatible with observed data and with a priori constraints. This scheme assumes an a priori statistical distribution $\pi_p(\mathbf{m})$ on the model parameters to be estimated, that synthesizes any data-independent information (e.g. constraints derived from physical laws). Information from observed data is modelled through the likelihood function $L(\mathbf{d} \mid \mathbf{m})$, which quantifies the degree of fit between the experimental system response and the theoretical one under the assumed validity of the generic model $\mathbf{m}$, as a function of the forward modelling $\mathbf{g}$. The posterior distribution $\sigma(\mathbf{m})$ is proportional to the product of the prior model and the likelihood function, thus combining information provided by measured data and by the physical theory (Tarantola & Valette 1982; Mosegaard & Tarantola 1995; Mosegaard & Sambridge 2002; Tarantola 2004):

$$\sigma(\mathbf{m}) \propto \pi_p(\mathbf{m})\, L(\mathbf{d}|\mathbf{m}). \tag{2}$$

Eq. (2) can be interpreted as the mapping of the measured data into a distribution of the desired model parameters. Therefore, it is a statistical representation of the solution of an inverse problem.

The main advantage of this formulation is that the derivation of information on estimated model parameters refers to the characterization of $\pi_p(\mathbf{m})$ and $L(\mathbf{d} \mid \mathbf{m})$, which is usually an easier task than describing $\sigma(\mathbf{m})$. Typical modelling describes $\pi_p(\mathbf{m})$ according to simple statistical schemes, for instance with a normal distribution

or a uniform model. $L(\mathbf{d} \mid \mathbf{m})$ usually depends on a misfit function $S(\mathbf{m})$, that measures the deviation between observed data and predicted data (Mosegaard & Tarantola 1995), the latter being often obtained through the forward problem:

$$L(\mathbf{d}|\mathbf{m}) \propto e^{-S(\mathbf{m})}. \tag{3}$$

The Monte Carlo procedure reconstructs $\sigma(\mathbf{m})$ through a two-step scheme. First, it simulates the prior distribution $\pi_p(\mathbf{m})$, drawing a suite of samples $\{\mathbf{m}_n\}$. As typical inverse problems adopt simple distribution models for $\pi_p(\mathbf{m})$, basic sampling methods allow an adequate simulation of it. Then, it computes the $L(\mathbf{d} \mid \mathbf{m})$ value for each sample $\mathbf{m}_n$, derived from the corresponding misfit $S(\mathbf{m}_n)$. In the inversion of surface wave data, $S(\mathbf{m}_n)$ compares experimental data [i.e. $V_R(\omega)$ and $\alpha_R(\omega)$] with the simulated values computed for each randomized earth model $\mathbf{m}_n$. The combination of the prior information and the likelihood value for each sample $\mathbf{m}_n$ returns samples of $\sigma(\mathbf{m})$, thus obtaining a suite of realizations for the posterior distribution.

3 SCALING PROPERTIES OF THE SOLUTION OF THE RAYLEIGH WAVE EIGENVALUE PROBLEM

Strobbia (2003), Socco & Strobbia (2004) and Maraschini *et al.* (2011) demonstrated that the modal solution in elastic conditions scales with the wavelength. Specifically, a scaling of V_S results in an equivalent scaling of both V_R and ω in the dispersion curve, whereas a scaling of H induces an inverse scaling of ω. In this study, it is demonstrated that this property can be extended to the linear viscoelastic model, thanks to the correspondence principle (Achenbach & Reddy 1967). In such conditions, a scaling of V_S and H leads to a scaling of $\alpha_R(\omega)$. As for variations in D_S, their mapping on the modal solution is non-trivial, but an approximate solution has been developed in this study. Although this approximation neglects the causality relationship between V_S and D_S (e.g. Christensen 2012), the resulting estimate is fairly accurate, as it will be shown in the final part of this section.

This section provides a synthetic and intuitive description of the scaling properties of the solution of the Rayleigh wave eigenvalue problem in viscoelastic conditions. However, a more detailed and mathematically rigorous demonstration is available in the online Supporting Information.

Let us consider a layered, viscoelastic earth model, wherein each layer is characterized by thickness H_0, P-wave velocity $V_{P,0}$, S-wave velocity $V_{S,0}$, P-wave damping ratio $D_{P,0}$, and S-wave damping ratio $D_{S,0}$. A harmonic Rayleigh wave with frequency f travels in this medium with a phase velocity $V_{R,0}$ and a phase attenuation $\alpha_{R,0}$ (alternatively, a phase damping ratio $D_{R,0}$—defined as $D_R \approx \alpha_R \times V_R/(2\pi f)$; Misbah & Strobbia 2014). On the other side, the propagation parameters of the R-wave mostly depend on the soil mechanical properties down to a depth approximately equal to the corresponding wavelength $\lambda = V_R/f$ (Foti 2000). Thanks to this property, variations in thicknesses, velocities, and damping ratios on the dispersion and attenuation curves can be mapped.

First, the effect of scaling V_S is investigated. Let us consider a soil model identical to the original one, but with layer velocities $V_{S,1}$ equal to $c \times V_{S,0}$, where c is a real constant. For a given wavelength λ, the corresponding R-wave phase velocity scales accordingly, therefore:

$$f_1 = \frac{V_{R,1}}{\lambda} = \frac{cV_{R,0}}{\lambda} = cf_0 \tag{4}$$

On the other hand, the corresponding R-wave phase attenuation is unaltered; indeed:

$$\alpha_{R,1} = \frac{2\pi f_1 D_{R,1}}{V_{R,1}} = \frac{2\pi c f_0 D_{R,0}}{cV_{R,0}} = \frac{2\pi f_0 D_{R,0}}{V_{R,0}} = \alpha_{R,0} \tag{5}$$

as $D_{R,1} = D_{R,0}$ because the damping ratio profile is not scaled. In summary, scaling all the S-wave velocities results in scaling both velocities and frequencies in the dispersion curve and frequencies only in the attenuation curve (Fig. 1).

Next, the effect of scaling H is investigated. In this case, the alternative soil model is characterized by layer thickness H_1 equal to $c \times H_0$, where c is a real constant. Thus, a Rayleigh wave of wavelength λ in the original medium and one of wavelength $\lambda_1 = c \times \lambda_0$ in the scaled medium both propagate with the same phase velocity $V_{R,0}$ and the same phase damping ratio $D_{R,0}$, as they are sampling a medium with the same characteristics. Therefore:

$$f_1 = \frac{V_{R,1}}{\lambda_1} = \frac{V_{R,0}}{c\lambda} = \frac{1}{c} f_0. \tag{6}$$

On the other hand, the corresponding R-wave phase attenuation is scaled in a similar way as the frequency; indeed:

$$\alpha_{R,1} = \frac{2\pi f_1 D_{R,1}}{V_{R,1}} = \frac{2\pi \frac{1}{c} f_0 D_{R,0}}{V_{R,0}} = \frac{1}{c}\frac{2\pi f_0 D_{R,0}}{V_{R,0}} = \frac{1}{c}\alpha_{R,0}. \tag{7}$$

In conclusion, scaling all the layers' thicknesses results in scaling frequencies only in the dispersion curve and both phase attenuations and frequencies in the attenuation curves (Fig. 2).

When scaling S-wave damping ratios, the resulting soil model is characterized by damping ratio $D_{S,1}$ equal to $c \times D_{S,0}$, where c is a real constant. For a given wavelength λ, the corresponding R-wave phase velocity (and frequency) is unchanged, whereas the corresponding phase attenuation is scaled:

$$\alpha_{R,1} = \frac{2\pi f_1 D_{R,1}}{V_{R,1}} = \frac{2\pi f_0 c D_{R,0}}{V_{R,0}} = c\frac{2\pi f_0 D_{R,0}}{V_{R,0}} = c\alpha_{R,0} \tag{8}$$

Therefore, scaling all the damping ratios results in an unchanged dispersion curve and in scaling phase attenuations in the attenuation curves (Fig. 3). However, this relationship is approximate because variations in D_S induce more complex modifications in the modal solution than a simple scaling. Indeed, variations in frequencies and phase velocities also occur, but there is no closed-form solution for predicting them. Furthermore, the modification in the attenuation is slightly non-linear and dependent on the frequency. However, such variations are rather small compared to the order of magnitude of phase velocities and frequencies of common applications, when dealing with low dissipative media. Therefore, the error induced by the approximation may be considered negligible, as also numerically shown by Armstrong *et al.* (2020).

4 PROPOSED MONTE CARLO ALGORITHM FOR THE JOINT INVERSION OF PHASE VELOCITY AND PHASE ATTENUATION CURVES

This section summarizes the main elements of the inversion procedure, that is the adopted prior model and likelihood function, and it provides a step-by-step description of the proposed algorithm.

This section includes the application of the proposed algorithm to retrieve the S-wave velocity and damping ratio profiles for two ideal profiles, namely a normally dispersive model (SW1) and a soil deposit with a low-velocity zone (SW2). Part I contains a detailed description of the two profiles. For both cases, we generated the

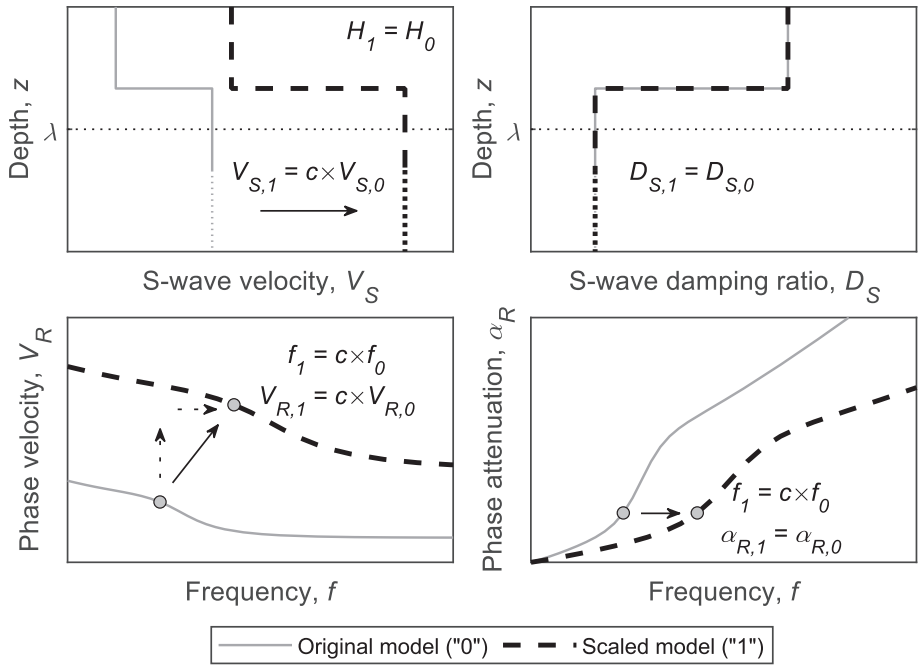

Figure 1. Effect of *S*-wave velocity scaling on the dispersion and attenuation curves.

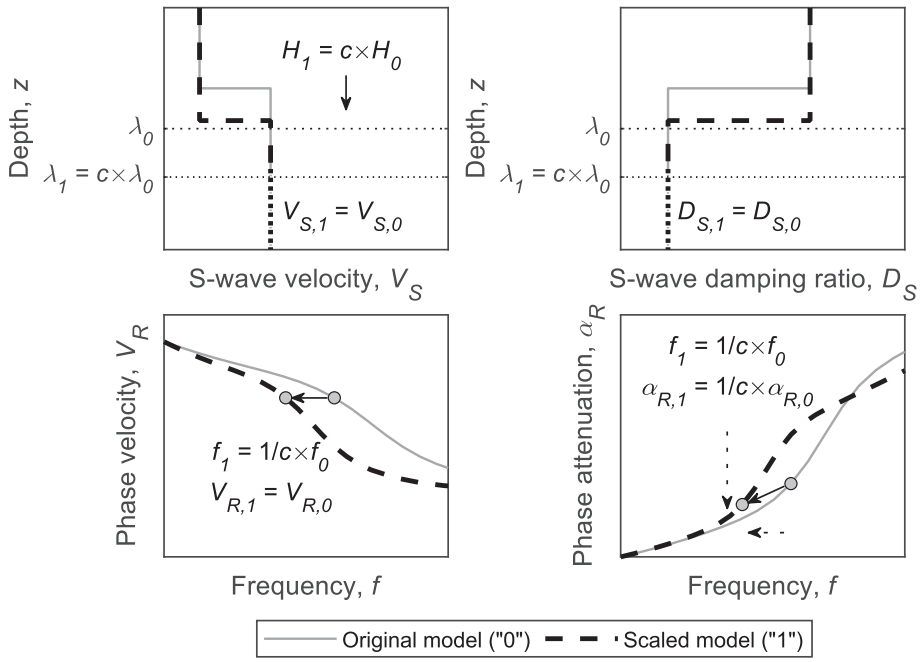

Figure 2. Effect of layer thickness scaling on the dispersion and attenuation curves.

inversion target by corrupting the theoretical fundamental mode dispersion and attenuation curves with Gaussian noise, thus creating a realistic data set which allows an effective assessment of the robustness of the proposed algorithm. Data variability was modelled according to a lognormal distribution for both the phase velocity and the phase attenuation (Aimar 2022). As for $V_R(\omega)$, the log-standard deviation was set to 0.05 at frequencies higher than 10 Hz and to 0.1 at lower frequencies. Both the trend with the frequency and the magnitude are compatible with the typical coefficient of variation (i.e. the ratio between the standard deviation and the mean) observed for dispersion data (Marosi & Hiltunen 2004; O'Neill 2004; Lai *et al.* 2005; Foti *et al.* 2009; Comina *et al.* 2011; Cox *et al.* 2014; Garofalo *et al.* 2016a; b; Olafsdottir *et al.* 2018; Teague *et al.* 2018a; b; Passeri *et al.* 2021)—note that the log-standard deviation and the coefficient of variation are similar when the corresponding values are small. Instead, the log-standard deviation for $\alpha_R(\omega)$ was set equal to five times the one for the velocity, consistently with results observed in the literature (Spang 1995; Rix *et al.* 2000; Verachtert 2018; Bergamo *et al.* 2019; Aimar 2022). Fig. 4 represents the fundamental mode (hereafter labelled as 'R0') $V_R(\omega)$ and $\alpha_R(\omega)$ data, and the error bars denote the interval defined by the median and one log-standard deviation. Data were computed at 30 log-spaced

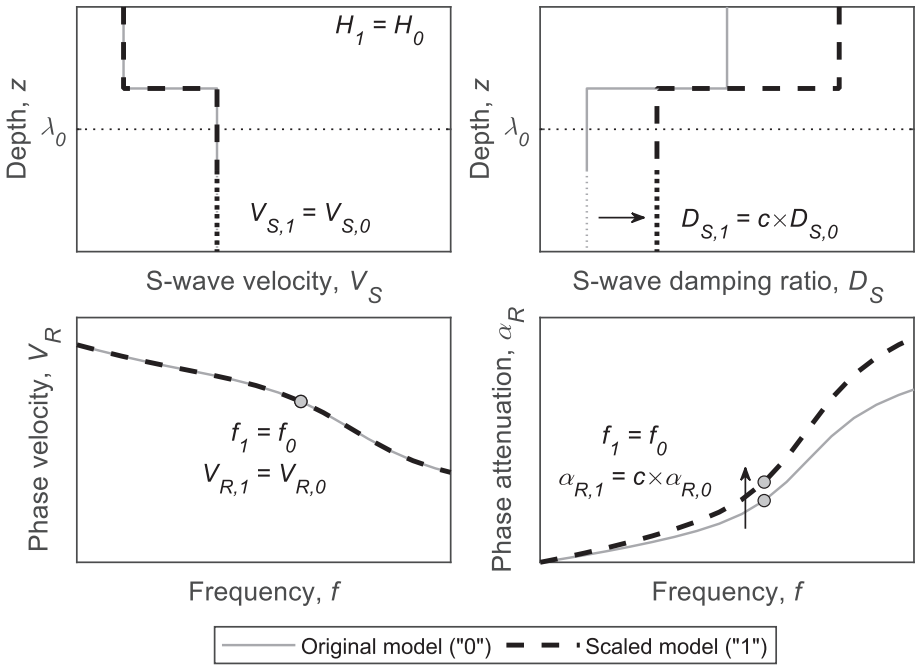

Figure 3. Effect of *S*-wave damping ratio scaling on the dispersion and attenuation curves.

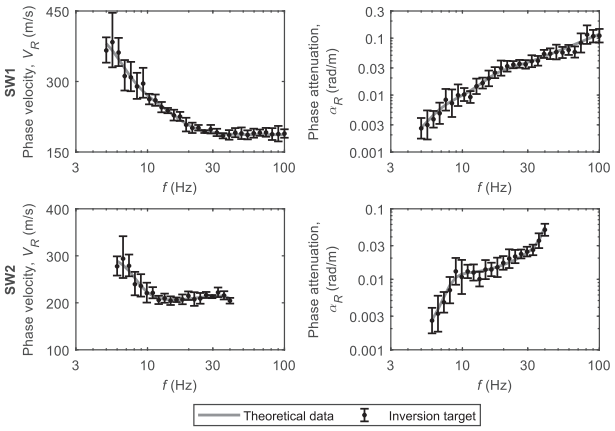

Figure 4. (a–b) Fundamental mode phase velocity (a) and phase attenuation (b) data obtained for the SW1 synthetic model perturbed with noise. (c–d) Fundamental mode phase velocity (c) and phase attenuation (d) data obtained for the SW2 synthetic model perturbed with noise. These data represent the target for the inversion procedure. Each panel includes information on the variability of the *R*-wave parameters, represented as error bars the width of which is related to the logarithmic standard deviation. Target dispersion and attenuation data are superimposed by the theoretical dispersion and attenuation curves for SW1 and SW2, for comparison purposes.

frequencies between 5 and 100 Hz (i.e. $\lambda = 2$–80 m) for SW1, and 20 log-spaced frequencies between 6 and 40 Hz (i.e. $\lambda = 5$–50 m) for SW2. The frequency ranges were selected to encompass a typical wavelength range investigated in MASW. However, in SW2, only data below 40 Hz were considered because R0 contributes to the wavefield only in this frequency range when considering a wavefield recorded according to a typical MASW setup (see Part I for further details). Therefore, *R*-wave parameters cannot be retrieved at higher frequencies. Furthermore, the adopted sampling grid, in terms of the sampling interval and the number of data points, complies with the recommendations provided by devoted guidelines (e.g. Foti *et al.* 2018; Olafsdottir *et al.* 2018; Vantassel & Cox 2021b).

4.1 Definition of the prior distribution

The Monte Carlo procedure requires the statistical characterization of the prior distribution $\pi_p(\mathbf{m})$, which collects the a priori knowledge on the model $\mathbf{m}$, corresponding to the unknown geometric and mechanical parameters (i.e. H, ρ, V_S, ν, D_S and D_P).

The adopted simulation procedure postulates that $\pi_p(\mathbf{m})$ is a multivariate, uniform distribution. The advantage of this assumption for $\pi_p(\mathbf{m})$ is multifold. On the one side, the statistical characterization of the parameter space can be carried out for every single model parameter in a separate way, and each one requires only two statistics for an exhaustive description (e.g. the boundaries of the uniform distribution). Furthermore, the generation of realizations $\{\mathbf{m}_n\}$ from $\pi_p(\mathbf{m})$ involves a sequential use of basic, 1-D sampling methods (Mosegaard & Sambridge 2002). Finally, for a uniform prior, $\sigma(\mathbf{m})$ is determined primarily by $L(\mathbf{d} \mid \mathbf{m})$, which, in turn, depends solely on the misfit function $S(\mathbf{m})$ (Sen & Stoffa 1996; Socco & Boiero 2008). Therefore, a characterization of $S(\mathbf{m})$ provides an adequate description of the posterior distribution, and inference on estimated ground models can be drawn from this quantity. For instance, the most suitable model [i.e. the one maximizing $\sigma(\mathbf{m})$] coincides with the minimum of $S(\mathbf{m})$.

Ideally, a proper definition of $\pi_p(\mathbf{m})$ requires an accurate definition of suitable ranges for all the ground model parameters. However, sensitivity studies demonstrated that each unknown parameter has a variable influence on the inversion process. Inversion results are mostly sensitive to H, V_S and D_S, whereas the role of ρ, V_P (or ν) and D_P is generally less relevant. Specifically, experimental data do not exhibit the same sensitivity to all the earth model parameters. On the one hand, modal dispersion data (i.e. V_R) strongly depend on H and V_S, whereas the influence of ρ and V_P (or ν) is generally negligible (Nazarian & Stokoe II 1984; Xia *et al.* 1999; Aki 2002; Badsar 2012; Verachtert 2018). Furthermore, D_S and D_P do not significantly impact their behaviour, at least in weakly dissipative media (Aki 2002; Badsar 2012; Verachtert 2018). On the other hand, modal attenuation data (i.e. α_R) are remarkably sensitive to H, V_S and D_S. The important role of V_S urges for robust inversion

schemes to retrieve an accurate stiffness model in order to achieve reliable D_S profiles. Instead, ρ and V_P (or ν) have a limited influence on attenuation curves. Finally, modal attenuation data are much less sensitive to D_P compared with D_S (Badsar 2012; Verachtert 2018).

A reasonable choice of the investigation range can mitigate solution non-uniqueness, improving the reliability and accuracy of the resulting ground models. For this purpose, geological data or independent geophysical and geotechnical surveys often provide valuable information that helps in optimizing the parameter choice (Foti *et al.* 2014; Teague *et al.* 2018a). These data often allow an effective constraint in the model layering (i.e. the number of layers in the ground model and their thickness). In case of unavailable site-specific information, it is strongly recommended to include variations in the inversion parametrization to account for epistemic uncertainty, for example through the layering ratio and/or the layering by number approaches (Cox & Teague 2016; Vantassel & Cox 2021b) or by including a statistical model for the layering (Passeri *et al.* 2020). Additionally, the interpretation of R0 experimental data allows to draw inference on the investigated parameters. Indeed, the transformation of the experimental dispersion curve from the V_R—f domain into the (1.05–1.1)$\times V_R$—λ/2.5 domain returns an approximation of the time-weighted average V_S profile as a function of the depth, the validity of which is stronger when R0 dominates the wavefield (Foti *et al.* 2014). The inspection of the transformed dispersion data provides some preliminary insights into the velocity structure of the medium, the minimum resolvable layer thickness, and the maximum investigable depth (Herrmann & Al-Eqabi 1991; Shtivelman 1999; Foti 2018). Similar considerations apply to the dissipation structure, which can be approximated by transforming experimental attenuation data from the α_R—f domain into the D_R—λ/2.5 domain. Indeed, the high-frequency phase damping ratio D_R usually matches the near-surface D_S, especially in normally dispersive media (e.g. Badsar 2012). However, the variation of D_R along the pseudo-depth usually does not allow an immediate inference of the dissipation structure of the medium, due to the great variability and the presence of oscillations linked with stiffness variations.

4.2 Definition of the likelihood function

According to eq. (3), the definition of the likelihood function $L(\mathbf{d} \mid \mathbf{m})$ is equivalent to the specification of a misfit function $S(\mathbf{m})$. This quantity is a distance metric between the observed data [i.e. $V_R(\omega)$ and $\alpha_R(\omega)$] and the predicted data, which are the values computed for each randomized earth model $\mathbf{m}_n$. The derivation of theoretical data requires the solution of the forward problem, corresponding to the Rayleigh-wave eigenvalue problem.

A popular definition of the misfit function assumes that the prediction error is normally distributed (Oldenburg & Li 2005). In this case, an effective metric to quantify model accuracy with respect to experimental data is the Mahalanobis distance (Mosegaard & Tarantola 1995), computed as the L2-norm of the prediction error vector, weighted by the experimental covariance matrix (Seber & Wild 2003). As experimental data are modelled according to a lognormal distribution and the linear correlation between measured $V_R(\omega)$ and $\alpha_R(\omega)$ is statistically insignificant (Aimar 2022), the following formulation for $S(\mathbf{m})$ can be used:

$$S(\mathbf{m}) = \frac{1}{2RW} \sum_{r=0}^{R-1} \sum_{w=1}^{W} \left[\frac{(\ln V_{w,\mathrm{R}r,e} - \ln V_{w,\mathrm{R}r,t})^2}{\sigma^2_{\ln V,w,\mathrm{R}r}} + \frac{(\ln \alpha_{w,\mathrm{R}r,e} - \ln \alpha_{w,\mathrm{R}r,t})^2}{\sigma^2_{\ln \alpha,w,\mathrm{R}r}} \right]. \quad (9)$$

The definition compares theoretical dispersion data $V_{w,\mathrm{R}r,t}$ and attenuation data $\alpha_{w,\mathrm{R}r,t}$ and observed median values $V_{w,\mathrm{R}r,e}$ and $\alpha_{w,\mathrm{R}r,e}$, normalized by the corresponding variances (i.e. $\sigma^2_{\ln V,w,\mathrm{R}r}$ and $\sigma^2_{\ln \alpha,w,\mathrm{R}r}$), for each considered propagation mode Rr and each frequency sample w (R is the number of modes and W is the number of data samples). Fig. 5 provides a graphical representation of the involved quantities. This structure of the misfit function is a least-square objective function, that can be interpreted as a generalization of the version often adopted in the model identification from phase velocity data (e.g. Wathelet *et al.* 2004). This definition separates the contributions linked with $V_R(\omega)$ and $\alpha_R(\omega)$ fitting, and the normalization with respect to the corresponding variance guarantees proportional weighting to dispersion and attenuation data. Therefore, the model identification accounts for the different degree of accuracy in observed data, also compensating for the different order of magnitude that characterizes $V_R(\omega)$ and $\alpha_R(\omega)$ (and the related prediction errors), thus avoiding potential overfitting of part of the observed data. The multiplying factor $1/2RW$ is an additional quantity that simply scales the $S(\mathbf{m})$ distribution without altering its shape, to provide a more intuitive interpretation of the numerical values of $S(\mathbf{m})$ itself. Indeed, $S(\mathbf{m})$ is unitary when the distance between predicted and experimental $V_R(\omega)$ and $\alpha_R(\omega)$ across the investigated frequency bandwidth and the considered propagation modes equals one standard deviation, on average. Furthermore, any model with $S(\mathbf{m})$ less than 1.0 fits the experimental data, on average, within one standard deviation or less.

4.3 Description of the algorithm

The proposed inversion procedure consists of a multistage operation, in which the most relevant steps are described below in detail. The steps are more concisely expressed in Algorithm 1. For easier understanding, the description includes results from the application of the algorithm to SW1 and SW2.

Step 1: Starting from the suite of experimental $V_R(\omega)$ and $\alpha_R(\omega)$ data (i.e. the inversion target), the procedure first defines the investigated ranges of each unknown parameter, thus specifying the prior model $\pi_p(\mathbf{m})$ assumed in the Monte Carlo procedure.

As for SW1 and SW2, the model identification adopts a fixed layering scheme, based on a three-layer ground model for SW1 and a two-layer profile for SW2. The layering is compatible with the stratigraphy of the corresponding synthetic profiles (see Part I). For simplicity, ρ is fixed at 2000 kg m^{-3} and ν is equal to 0.3, and D_P is assumed as equal to D_S, consistently with the assumed values used for the generation of the synthetic wavefields. However, the investigated ranges of H, V_S and D_S were kept moderately large, spanning a broader range compared with potential constraints informed by the target inversion data, converted into the 1.1 $\times$ V_R—λ/2.5 and the D_R—λ/2.5 domains. These ranges are shown in Table 1. The ranges were kept the same in all the layers and no constraints on velocity and damping ratio variations between subsequent layers were applied, although they could have been deduced from the target data. In this way, the robustness of the proposed inversion algorithm can be effectively tested, since the influence of a priori assumptions on the inversion results is reduced.

Step 2: Then, the Monte Carlo procedure simulates the prior distribution $\pi_p(\mathbf{m})$, drawing a suite of samples $\{\mathbf{m}_n\}$. This task is achieved by randomly extracting each model parameter [i.e. H, ρ, V_S, ν, D_S and D_P] from a uniform distribution, the range of which has been defined in the previous step. The corresponding ground models represent samples of $\pi_p(\mathbf{m})$. In this study, the inversion was run generating 10 000 trial earth models.

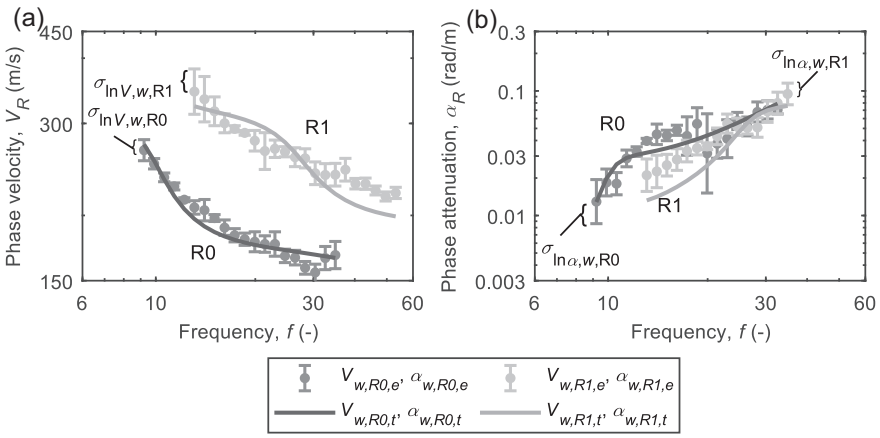

Figure 5. Quantities involved in the definition of the misfit function $S(\mathbf{m})$, namely theoretical estimates (subscript 't') and observed data (subscript 'e'). This example refers to an experimental data set characterized by two R-wave propagation modes (after Aimar 2022).

Algorithm 1: Monte Carlo algorithm for the joint inversion of phase velocity and phase attenuation.

Input: $\{V_{w,\mathrm{R}r,e}, \sigma_{\ln V,w,\mathrm{R}r}, \alpha_{w,\mathrm{R}r,e}, \sigma_{\ln \alpha,w,\mathrm{R}r}\}_{r=1,w=1}^{R,\,W}$: experimental modal phase velocity and phase attenuation data (median values and variability), for R modes r, at W frequency samples ω_w

Assumed the number of layers L, define investigation ranges for H_l, ρ_l, $V_{S,l}$, $V_{P,l}$ (or ν_l), $D_{S,l}$ and $D_{P,l}$, with $l = 1,\ldots, L$

Generate random trials of H_l, ρ_l, $V_{S,l}$, $V_{P,l}$ (or ν_l), $D_{S,l}$ and $D_{P,l}$ ($l = 1,\ldots, L$), according to a uniform distribution, for N profiles n

for $n = 1 : N$ **do**

  Solve Rayleigh eigenvalue problem:
  $\{H_{l,n}, \rho_{l,n}, V_{S,l,n}, V_{P,l,n}, D_{S,l,n}, D_{P,l,n}\}_{l=1}^{L} \rightarrow \{V_{w,\mathrm{R}r,t}, \alpha_{w,\mathrm{R}r,t}\}_{r=1,w=1}^{R,\,W}$

  Identify scaling factors to minimize $S(\mathbf{m}_n)$, defined in eq. (9): $\{c_{f,n}, c_{VR,n}, c_{\alpha R,n}\} \leftarrow \mathrm{argmin} S(\mathbf{m}_n)$
  Calculate $\{c_{H,n}, c_{VS,n}, c_{DS,n}\}$ from $\{c_{f,n}, c_{VR,n}, c_{\alpha R,n}\}$ through eq. (10)

  Modify profile parameters and corresponding theoretical R-wave parameters:
  $\{H_{l,n}, \rho_{l,n}, V_{S,l,n}, V_{P,l,n}, D_{S,l,n}, D_{P,l,n}\}_{l=1}^{L} \leftarrow \{c_{H,n} H_{l,n}, \rho_{l,n}, c_{VS,n} V_{S,l,n}, c_{VS,n} V_{P,l,n}, c_{DS,n} D_{S,l,n}, c_{DS,n} D_{P,l,n}\}_{l=1}^{L}$
  $\{V_{w,\mathrm{R}r,t}, \alpha_{w,\mathrm{R}r,t}\}_{r=1,w=1}^{R,\,W} \leftarrow \{c_{VR,n} V_{w,\mathrm{R}r,t}(c_{f,n}\omega_w), c_{\alpha R,n}\alpha_{w,\mathrm{R}r,t}(c_{f,n}\omega_w)\}_{r=1,w=1}^{R,\,W}$

  Compute misfit $S(\mathbf{m}_n)$, defined in eq. (9)

end for

Select a number of lowest misfit soil profiles to quantify uncertainty

Output: Collection of S-wave velocity V_S and S-wave damping ratio D_S profiles, compatible with experimental Rayleigh wave modal dispersion curves and attenuation curves

Table 1. Boundaries of the investigated parameter domain for the inversion of SW1 and SW2 data.

Model	Thickness, H (m)	S-wave velocity, V_S (m s^{-1})	S-wave damping ratio, D_S (per cent)
SW1	1–15	100–600	1–7
SW2	1.5–10	100–500	0.5–7

Step 3: For each randomized earth model $\mathbf{m}_n$, theoretical dispersion data $V_{n,\mathrm{R}j,t}$ and attenuation data $\alpha_{n,\mathrm{R}j,t}$ are computed. The derivation of theoretical values requires the solution of the forward problem, corresponding to the Rayleigh-wave eigenvalue problem. This operation is herein carried out through the ElastoDynamics Toolbox (EDT; Schevenels *et al.* 2009), which implements the transfer matrix method (Thomson 1950; Haskell 1953). The implemented algorithm estimates the modal complex dimensionless wavenumber (normalized by the frequency) using a search algorithm that minimizes the determinant of the stiffness matrix of the medium, simultaneously tracking changes in modal shapes with the frequency to avoid undesired jumps to a different mode. Then, the dispersion and attenuation curves are obtained from the complex wavenumber. Additional details can be found in Schevenels *et al.* (2009) and the software is available at https://bwk.kuleuven.be/bwm/edt.

Step 4: The scaling properties are then used to modify the random samples so that the theoretical data better match observed values. Specifically, for each trial ground model, the predicted dispersion and attenuation data are scaled to improve the fitting with the experimental values, and the corresponding model parameters are modified through the inverse application of the scaling properties. This application in the elastic inversion procedure was introduced by Socco & Boiero (2008), where the scaling of the theoretical data was based on the comparison of the gravity centres between predicted and observed dispersion data. In this study, the scaling procedure jointly modifies the theoretical frequencies, phase velocities, and phase attenuations according to three scaling coefficients (labelled as c_f, c_{VR} and $c_{\alpha R}$, respectively), that are calibrated through a local optimization procedure which minimizes the discrepancy between theoretical and experimental data, measured by misfit function $S(\mathbf{m})$ introduced in eq. (9). Compared with measuring the distance on the gravity centre only, the proposed approach does not only guarantee a good matching between scaled and observed data at the gravity centre, but it also introduces a constraint on the behaviour of the

remaining points. Therefore, the estimated scaling coefficients also account for the geometry of the dispersion and attenuation data, thus ensuring better matching between predicted and experimental data. Once the scaling factors c_f, c_{VR} and $c_{\alpha R}$ are obtained, the corresponding scaling factors for layer thicknesses (c_H), *S*-wave velocities (c_{VS}) and *S*-wave damping ratios (c_{DS}) are computed as follows:

$$c_H = \frac{c_{VR}}{c_f},\ c_{VS} = c_{VR},\ c_{DS} = \frac{c_{VR}}{c_f} c_{\alpha R}\,. \tag{10}$$

By applying these scaling factors to the corresponding parameters, each trial earth model is converted into a new one, whose theoretical *R*-wave parameters better match the experimental ones.

Step 5: Finally, the ranking of each trial scaled model with respect to observed data is quantified by the misfit function $S(\mathbf{m})$ introduced in eq. (9).

Step 6: The last step of the inversion procedure consists of the selection of a representative suite of ground models to describe inversion results. This set should ensure an adequate matching with experimental data (i.e. low misfit) and account for the uncertainties both in the inversion problem (due to solution non-uniqueness) and in the experimental data themselves (Mosegaard & Sambridge 2002). For this purpose, various approaches have been proposed for the inversion of phase velocity data (e.g. Socco & Boiero 2008; Griffiths *et al.* 2016; Hallo *et al.* 2021). However, currently, there are no methods for identifying a reference collection of samples from the joint inversion of phase velocity and phase attenuation data. Furthermore, the generalization of existing criteria to select adequate damping models is not immediate because this should account for both the multivariate nature of the joint inversion and the different degree of variability affecting experimental data. In the context of Bayesian inversion, an effective strategy relies on specific statistics extracted from the posterior distribution (Hallo *et al.* 2021). Alternatively, a non-conventional, yet intriguing approach directly obtains the desired distribution by running multiple inversion simulations on a suite of experimental data, whose statistical features are compatible with measured ones (Vantassel & Cox 2021a). This study adopts a simple strategy, reporting a collection of best-fitting models as the representative suite. Despite its simplicity, this selection criterion provides insight into the main features of inverted models and the related uncertainties.

Fig. 6 shows the results for the 30 best-fitting models obtained from the inversion of the SW1 data set, whereas results for SW2 are represented in Fig. 7. In both cases, inverted S-wave velocity profiles are tightly grouped, with a clearly identifiable velocity structure. As for D_S, the estimated profiles are affected by larger variability, which increases with depth. This is an effect of the high $\sigma_{\ln\alpha}$ in the experimental data, that does not allow a constraint on D_S as effectively as in the stiffness modelling. However, inverted profiles exhibit a quite clear trend, with variations compatible with those of the theoretical profiles, especially when focusing on the lowest misfit profile. Notably, in SW1, the variability of the estimated V_S and D_S is small in the near-surface layer, perhaps because of the constraint exerted by the large number of data available at high frequencies (hence, short wavelengths). For this reason, in SW2, the near-surface D_S variability is larger than the one observed in SW1, although the estimated V_S profiles almost perfectly match the theoretical model and the assumed data variability is the same, because of the lack of target data at high frequencies.

These qualitative results support the effectiveness of the proposed inversion algorithm, which manages to retrieve V_S and D_S compatible with the theoretical ones. As expected, the matching is not perfect because of the noise perturbation on the inversion target combined with the limited wavelength range available from the target data and the large ranges in the investigated parameter domain. Nonetheless, the procedure manages to consistently retrieve the expected profiles, with moderately limited computation effort. This aspect will be addressed in detail in the next section, which also includes a quantitative assessment on the quality of inversion results.

4.4 Discussion

A key step in the proposed inversion algorithm is the implementation of the scaling properties of the Rayleigh eigenvalue problem in linear viscoelastic media. This strategy strongly mitigates one critical aspect of Monte Carlo-based global search methods, which is the need to effectively sample the investigated parameter space. Indeed, as the search domain is broad and high-dimensional, a huge number of model realizations is required to minimize the risk of neglecting promising regions. However, increasing the number of generated models means a greater number of forward simulations, entailing a significant rise in computation time. The computation burden is even more relevant when viscoelastic media are involved, due to the greater complexity of the forward algorithm. As an example, the performance of elastic and viscoelastic forward modelling codes are compared, with reference to the computation of modal $V_R(\omega)$ and $\alpha_R(\omega)$ for SW1, at 82 frequencies spanning between 0.5 and 100 Hz. Elastic modelling was carried out through MATLAB codes, whereas the EDT toolbox (Schevenels *et al.* 2009) was used for viscoelastic simulations. Numerical calculations were run on a workstation, with 24 Intel® Xeon® W-2265, 3.50 GHz CPUs. The computation time needed for computing fundamental-mode data is 0.15 s in elastic conditions and 0.9 s when computing both $V_R(\omega)$ and $\alpha_R(\omega)$ in viscoelastic conditions. If the goal of the forward simulation is estimating the first two *R*-wave modes (e.g. for multimode inversion), elastic modelling takes 0.45 s, whereas the computation time is 2.3 s in viscoelastic conditions. Therefore, viscoelastic forward modelling is 5–6 times more time-consuming than the corresponding elastic computation. This dramatically affects the global search procedure, as the number of trial earth models should not be large, to avoid excessively time-consuming inversion runs. For instance, running a viscoelastic inversion stage with 10^4 trial ground models needs about 12–24 hr for being completed, depending on the size of the parameter space and the number of propagation modes being simulated. Often, elastic inversion studies involve 10^5–10^7 trial models (i.e. the typical sample size used in the inversion of phase velocity data), which would require a time that is incompatible with practical needs for viscoelastic inversions. On the other side, reducing the number of random samples hinders the capacity of the search algorithm to explore the parameter space, increasing the risk of discarding potentially good solutions.

The scaling properties of the solution of the Rayleigh wave eigenvalue problem represent a valuable tool to optimize the generated Monte Carlo samples, with negligible increase in computation time. Indeed, these properties can be used to modify the random samples so that the theoretical data better match observed values. The result of the scaling procedure is an alternative sampling of the parameter space, with the models concentrated in the high-probability region, which is closer to the true model (Socco & Boiero 2008). This allows to optimize the sampled portion, converting the set of trial earth models into an alternative one better suiting observed data. In this way, the number of required samples (hence, forward

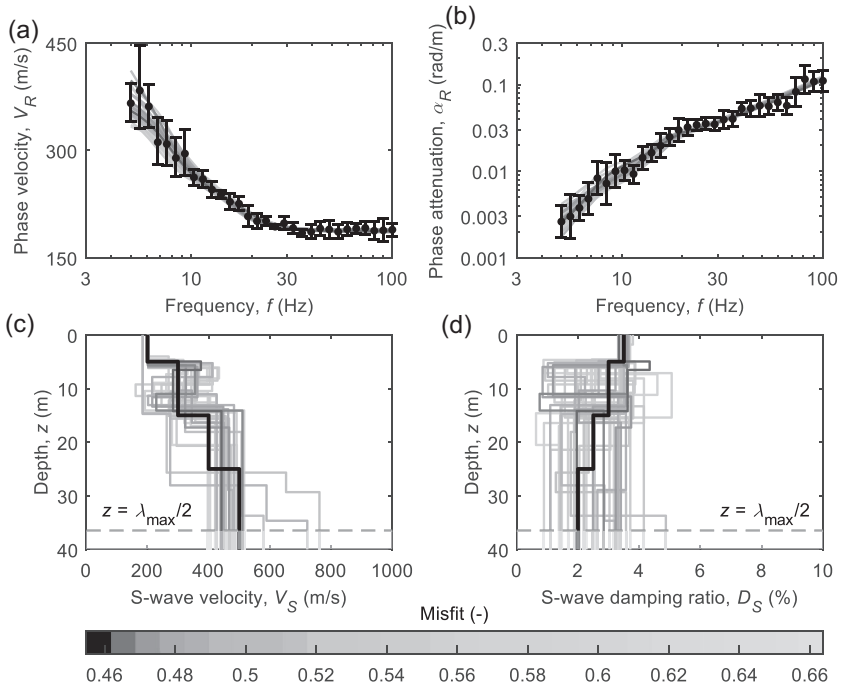

Figure 6. Best-fitting ground models to SW1 data: (a–b) Theoretical versus target data, for the phase velocity (a) and phase attenuation (b). (c–d) Resulting *S*-wave velocity (c) and damping ratio (d) profiles. The boundary $z = \lambda_{max}/2$ is an approximated value of the maximum investigable depth, that can be achieved from the available experimental data–layer interfaces beneath it are usually less reliable. The theoretical *S*-wave velocity and damping ratio profiles are represented with a thick black line.

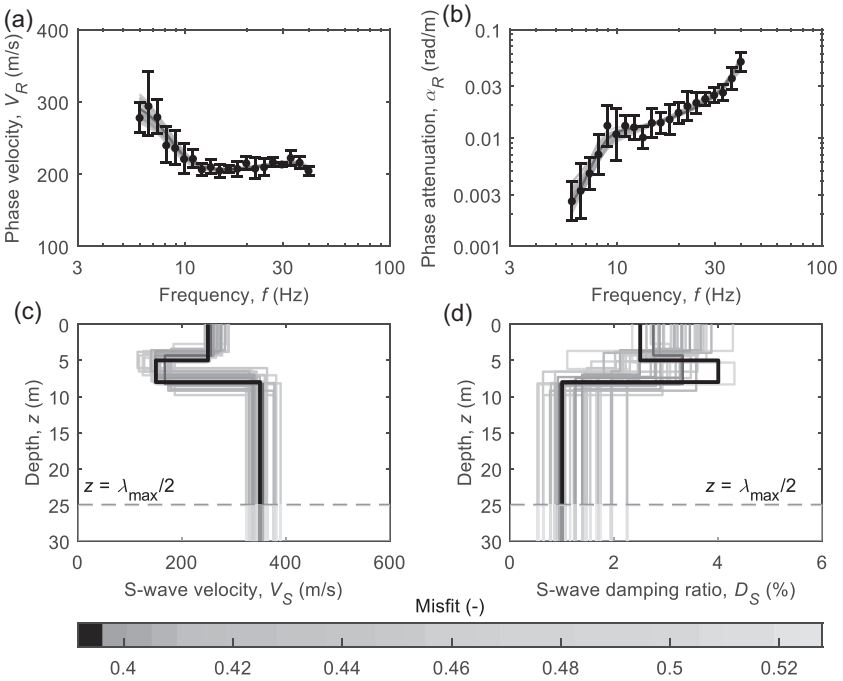

Figure 7. Best-fitting ground models to SW2 data: (a–b) theoretical versus target data, for the phase velocity (a) and phase attenuation (b). (c–d) Resulting *S*-wave velocity (c) and damping ratio (d) profiles. The boundary $z = \lambda_{max}/2$ is an approximated value of the maximum investigable depth, that can be achieved from the available experimental data–layer interfaces beneath it are usually less reliable. The theoretical *S*-wave velocity and damping ratio profiles are represented with a thick black line.

simulations) can be significantly reduced, thus saving computation time.

To test the benefits achievable with the scaling properties, SW1 and SW2 data sets were also inverted through a 'standard' Monte Carlo procedure, in which the scaling properties are not applied. For the sake of comparison, the inversion started with the same collection of trial profiles. Then, the quality of inversion results was quantified by measuring the average relative error $\bar{\varepsilon}_{VD}$ between the

estimated V_S and D_S profiles—$V_{S,e}$ and $D_{S,e}$, respectively—and the theoretical V_S and D_S profiles:

$$\bar{\varepsilon}_{VD} = \frac{1}{Z}\sum_{z=1}^{Z}\left(\frac{|V_{S,e} - V_S|}{V_S} + \frac{|D_{S,e} - D_S|}{D_S}\right) \quad (11)$$

This error is computed over the resolvable depth range based on the target inversion data—for simplicity, assumed as equal to $\lambda_{max}/2$, with λ_{max} being the maximum wavelength—and considering a depth grid with size equal to 0.5 m, with a total of Z depth bins.

Considering the lowest-misfit profile for SW1, the computed estimation errors $\bar{\varepsilon}_{VD}$ are 0.46 for the 'standard' Monte Carlo procedure and 0.12 for the proposed inversion algorithm. Instead, for SW2, $\bar{\varepsilon}_{VD}$ is 0.24 for the 'standard' Monte Carlo procedure and 0.062 for the proposed inversion algorithm. Notably, the average error reduces with a factor of 5 when the proposed inversion scheme is used. Furthermore, for both SW1 and SW2, $\bar{\varepsilon}_{VD}$ is less than 0.15, that is the deviation between estimated and the theoretical V_S and D_S profiles is about 15 per cent, on average. Therefore, high-quality inverted profiles can be obtained even with a relatively small number of trial earth models as the one assumed in this study (i.e. 10 000 models).

In addition, the performance of the proposed, coupled inversion algorithm was also tested against the uncoupled inversion approach, based on a separate inversion of $V_R(\omega)$ and $\alpha_R(\omega)$ (e.g. Rix *et al.* 2000; Xia *et al.* 2002; Xia *et al.* 2012). Specifically, the uncoupled algorithm was applied to obtain the best-misfit velocity profile, which was then used as reference for the damping inversion, in which the lowest-misfit model with respect to the target $\alpha_R(\omega)$ was finally extracted. For the uncoupled procedure, the computed estimation errors $\bar{\varepsilon}_{VD}$ are 0.19 for SW1 and 0.075 for SW2 (against 0.12 and 0.062, respectively). This is due to the error amplification that occurs in the sequential scheme (Lai & Rix 1998). Furthermore, the joint inversion accounts for the intrinsic coupling between the *R*-wave phase velocity and phase attenuation in linear, viscoelastic media, that derives from the Cauchy–Riemann equations (Lai & Rix 1998; Lai *et al.* 2002). This introduces an additional constraint on the selection of the trial models, which further mitigates the ill-posedness of the inversion problem and improves the quality of the estimated soil models.

These examples (as well as the application in the next section) address the performance of the proposed algorithm for the inversion of fundamental mode data only, although the formulation allows for the handling of multimode experimental data sets. Indeed, the main scope of this paper is to demonstrate the potential of the joint inversion and the effectiveness of implementing the scaling properties to optimize inversion results. The complexity of the topic suggests limiting the present discussion leaving out the inclusion of multiple modes. However, data from higher modes provide additional independent information that improves the degree of constraint of the inverse problem (Foti *et al.* 2018). Therefore, the joint inversion of multimode data may help to improve the quality of the estimated soil models by reducing their variability and increasing the investigated depth (e.g. Gabriels *et al.* 1987). On the other hand, it should be noted that the benefits of multimode inversion have been demonstrated only for the inversion of velocity data, whereas the advantages on the combined inversion of velocity and attenuation data need to be further investigated in future studies.

5 APPLICATION OF THE INVERSION ALGORITHM TO A REAL SITE: THE GARNER VALLEY DOWNHOLE ARRAY

This section describes the application of the proposed algorithm to retrieve the *S*-wave velocity and damping ratio profiles at the Garner Valley Downhole Array (GVDA) site, where a MASW survey was carried out. Part I contains a detailed description of the GVDA site, together with the MASW survey and the estimation of *R*-wave parameters. Fig. 8 represents the fundamental mode ('R0') $V_R(\omega)$ and $\alpha_R(\omega)$ data computed through the CFDBFa method, and the error bars denote the interval defined by the mean and one log-standard deviation. These statistics were inferred from the elementary *R*-wave parameters corresponding to different source offsets, in consistency with the multi-offset approach (Wood & Cox 2012; Vantassel & Cox 2022), assuming a lognormal distribution of the experimental data (Aimar 2022). Data are computed at log-spaced frequencies between 5 and 35 Hz (i.e. λ = 5–90 m). This represents the target data set used in the inversion procedure.

Starting from the suite of experimental $V_R(\omega)$ and $\alpha_R(\omega)$ data (i.e. the inversion target), the investigated ranges of each unknown parameter were defined, and they are summarized in Fig. 9 and Table 2. In order to mitigate non-uniqueness, ρ is fixed at typical values compatible with the lithology and the location of the water table (Foti & Strobbia 2002; Foti *et al.* 2018) and D_P is assumed as equal to D_S. The investigated ranges of H, V_S and D_S were mainly informed by the experimental data, converted into the $1.1 \times V_R$—$\lambda/2.5$ and the D_R—$\lambda/2.5$ domains (refer to Fig. 9) so they could more easily be related to the V_S and D_S profiles. The explored parameter space includes models with the half-space interface at around 40 m. This depth is consistent with $\lambda_{max}/2$ (where λ_{max} is the maximum wavelength), that is a conservative proxy of the maximum investigable depth, within which layer interfaces should be located (Foti *et al.* 2014). Both the surface geology and invasive testing (e.g. Gibbs 1989; Steller 1996; Teague *et al.* 2018b) demonstrated the presence of a low-velocity alluvium layer overlying weathered rock, with remarkably greater stiffness. Therefore, the model identification adopts a fixed layering scheme, based on a four-layer ground model. The parametrization includes three shallow layers with moderately low V_S, which gradually increases with depth. These layers seek to capture V_S variations in the alluvium, as suggested by the gradual rise of $1.1 \times V_R$ with $\lambda/2.5$. Note that the search domain also includes a near-surface thin layer, with a thickness slightly below the minimum resolvable value according to experimental data (i.e. $\lambda_{min}/3 = 1.8$ m, where λ_{min} is the minimum wavelength; Foti *et al.* 2014). Indeed, the shallow D_R exhibits a remarkable increase, without achieving a stable value. Therefore, it is assumed that the presence of a thin, highly dissipative layer might be responsible for such behaviour. It is assumed that the half-space is likely representative of weathered rock, for which the average V_S of the investigated range sensibly increases. On the other hand, not enough information is available to constrain D_S at depth. Therefore, the investigated ranges are rather broad to ensure an adequate exploration of the parameter space. However, a gradual reduction of D_S with depth is accommodated, to comply with the gradual decrease of D_R when $\lambda/2.5$ is large. Finally, the parametrization also allowed independent randomization for V_P, of which ranges were based on PS-logging data carried out at the GVDA (Steller 1996). Also, to ensure realistic coupling with V_S, ν was constrained within realistic boundaries. As the available geological and geophysical information indicates

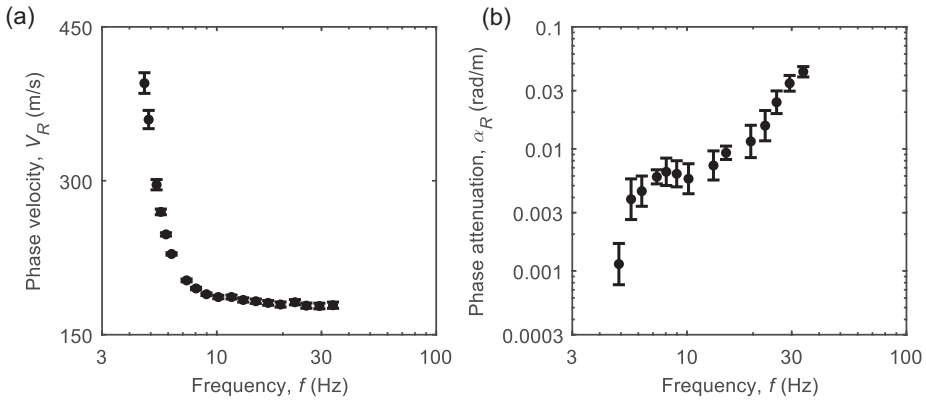

Figure 8. Experimental phase velocity (a) and phase attenuation (b) data at the GVDA site.

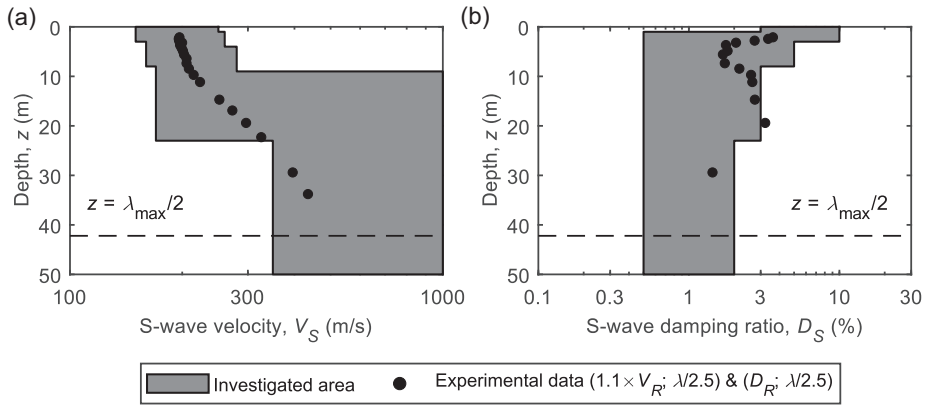

Figure 9. Range of V_S and D_S profiles corresponding to the investigated parameter domain, reported in Table 2. The search domain is overlapped by the 'pseudo-depth' representation of experimental data, that is 1.1 × V_R versus λ/2.5 and D_R versus λ/2.5.

Table 2. Boundaries of the investigated parameter domain for the inversion of GVDA data.

Layer	Thickness, H (m)	Mass density, ρ (kg m^{-3})	S-wave velocity, V_S (m s^{-1})	P-wave velocity, V_P (m s^{-1})	Poisson ratio ν (-)	S-wave damping ratio, D_S (per cent)	P-wave damping ratio, D_P (per cent)
1	1–3	1600	150–250	300–500	0.25–0.40	1–3	Equal to D_S
2	3–5	1600	160–260	320–520	0.25–0.40	0.05–5	Equal to D_S
3	5–15	1750	170–280	1350–1650	0.43–0.49	0.03–5	Equal to D_S
Half-space	-	2000	350–1000	1800–3000	0.43–0.49	0.03–2	Equal to D_S

the location of the groundwater table at a depth of about 5 m (e.g. Hill 1981; Steller 1996), the assumed ν increases in the deeper layers to account for soil saturation (Foti & Strobbia 2002; Foti *et al.* 2018). In general, the search domain is broad enough to allow an effective exploration of the parameter domain and to accommodate for discrepancies from *a priori* information. However, it should be remarked that the adopted boundaries only represent the parameter space for the generation of the trial population. The application of the scaling properties in the next stage may allow models to move outside such boundaries (e.g. Socco & Boiero 2008).

The inversion was run generating 10 000 trial earth models and Fig. 10 shows the 30 best-fitting models obtained from the inversion of the GVDA data set. Regarding the *S*-wave velocity, the inversion provided a clearly identifiable velocity structure. Specifically, the resulting V_S model includes a low-velocity near-surface portion, with V_S close to 200 m s^{-1}. Then, it suddenly increases to 450–500 m s^{-1} at around 18 m of depth, which is compatible with the location of the interface between alluvium and weathered rock (see Part I). As for D_S, the estimated profiles are affected by larger variability, which increases with depth. This is an effect of the high $\sigma_{\ln\alpha}$ in the experimental data, that does not allow a constraint on D_S as effectively as in the stiffness modelling. However, inverted profiles exhibit a quite clear trend, characterized by D_S of approximately 5 per cent in the near-surface layer, which decreases to about 1 per cent in the underlying layer. The large D_S in the shallow portion of the ground models might be an effect of heterogeneities on the top of the soil deposit, which have been also identified in Fathi *et al.* (2016). Lateral variations result in wave scattering phenomena, that induce an apparent increase of D_S.

An insight into the reliability of estimated ground models can be obtained by comparing the resulting V_S and D_S profiles with those estimated in alternative *in situ* characterization studies conducted at the GVDA site. Fig. 11 overlaps the estimated earth models with the results of previous studies (Gibbs 1989; Steller 1996; Brown

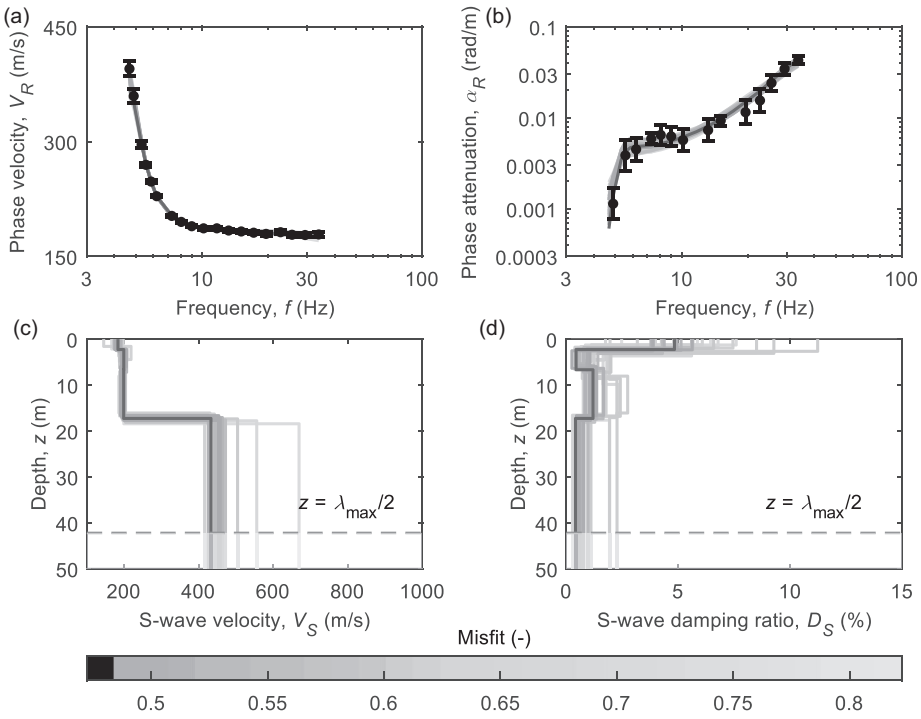

Figure 10. Best-fitting ground models to GVDA experimental data: (a–b) theoretical versus experimental data, for the phase velocity (a) and phase attenuation (b). (c–d) Resulting *S*-wave velocity (c) and damping ratio (d) profiles. The boundary $z = \lambda_{max}/2$ is an approximated value of the maximum investigable depth, that can be achieved from the available experimental data–layer interfaces beneath it are usually less reliable.

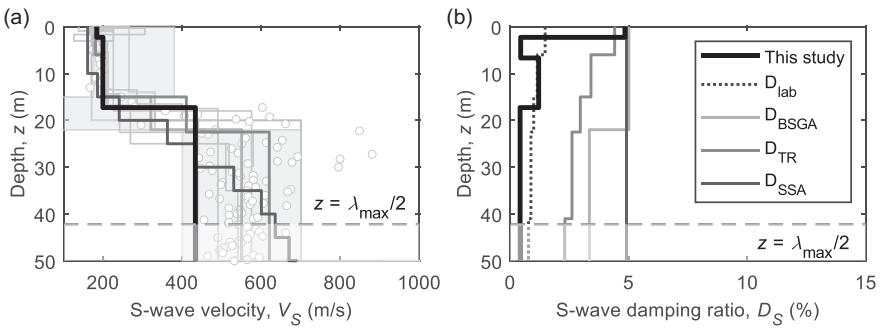

Figure 11. Comparison between the best-fitting ground model to GVDA experimental data and velocity and damping ratio models obtained in past studies: (a) *S*-wave velocity profiles; (b) *S*-wave damping ratio profiles. Results from past studies include data from PS suspension logging (i.e. the grey circular symbols; Steller 1996), downhole and surface wave testing (i.e. the thin grey lines; Gibbs 1989; Brown *et al.* 2002; Stokoe II *et al.* 2004; Teague *et al.* 2018b), and seismic interferometry (i.e. the grey region; Chandra *et al.* 2015). The remaining lines correspond to the models labelled as D_{lab}, computed according to Darendeli (2001); D_{BSGA}, proposed by Bonilla *et al.* (2002); D_{TR}, proposed by Tao & Rathje (2019) and D_{SSA}, proposed by Seylabi *et al.* (2020).

et al. 2002; Stokoe II *et al.* 2004; Chandra *et al.* 2015; Teague *et al.* 2018b; Seylabi *et al.* 2020). Fig. 11(b) includes a laboratory-based D_S estimate, which has been obtained through the Darendeli (2001) empirical model. This value should provide a measure of intrinsic material damping, which is usually overestimated by *in situ* damping values due to the presence of additional attenuation mechanisms (e.g. geometric attenuation and seismic wave scattering; Foti 2003; Tao & Rathje 2019). This component typically affects *in situ* estimates, due to the difficulty in separating geometric and intrinsic attenuation, that is the energy loss due to wavefront expansion and to wave scattering in heterogeneous media, on one side, and the one due to intrinsic material attenuation, on the other. It also shows the D_S models proposed by Bonilla *et al.* (2002), Tao & Rathje (2019) and Seylabi *et al.* (2020), which were estimated from the interpretation of downhole array data available at the GVDA site.

In general, the resulting V_S profiles well match other studies in the near-surface layers, with good consistency both in terms of stiffness values and the depth of the impedance variation. The latter is also compatible with site geology. However, some divergence occurs for the V_S values below 20 m, which should be representative of the weathered rock unit. Indeed, this study returned $V_S = 450$–$500\ \mathrm{m\ s^{-1}}$, whereas past studies provided larger V_S values, spanning between 450 and 600 $\mathrm{m\ s^{-1}}$. This discrepancy may be justified as an effect of lateral variability at the GVDA site, which results in significant variations of V_S at intermediate depths, as also highlighted by the large variations in results from past studies (Teague *et al.* 2018b).

As for D_S, the estimated damping model is compatible with the laboratory-based profile, especially at intermediate depths. However, it should be remarked that the latter is not specific to this site, as

it derives from an empirical model which provides an average damping ratio for typical fine-grained soil deposits. Therefore, no strong conclusions can be drawn from this comparison. On the other hand, the consistency between these two alternative schemes suggests that the MASW-based D_S estimate shares the same order of magnitude of the material damping ratio, hence the influence of scattering is not strongly significant—at least, in the depth range investigated in this survey. Actually, the laboratory-based D_S is significantly different in the shallow layer. This discrepancy may be an effect of local heterogeneities and near-surface variability demonstrated in alternative studies (e.g. Fathi *et al.* 2016), which is responsible of additional attenuation mechanisms other than intrinsic dissipation, that induce significant scattering of high-frequency Rayleigh waves. Indeed, as they propagate with moderately small wavelengths, they are rather sensitive to local fluctuations in the soil deposit characteristics. These considerations also explain why the inverted D_S models from this study are significantly lower than the values proposed by Bonilla *et al.* (2002), Tao & Rathje (2019) and Seylabi *et al.* (2020), except in the shallow layer. Indeed, these results derive from the interpretation of down-hole array data recorded at the GVDA from both shallow and deep sensors, involving a depth range much broader than the one investigated in this survey. Therefore, such estimates rely on large-scale variations, which include different impedance variations and additional dissipation mechanisms than material damping, such as wave scattering and reflection/refraction phenomena at the layer interfaces. This results in increased attenuation. Indeed, it is expected that these phenomena are quite relevant at the GVDA site, as spatially variable mechanical properties and the consequent anisotropy in the velocity structure are significant, especially at intermediate-to-large depths layers (Coutant 1996; Bonilla *et al.* 2002). The influence of lateral variability and the different volume of sampled soil (in terms of investigated depth and lateral extent) as a function of the characterization technique needs to be addressed in future studies, to get better insight on the reasons behind such discrepancies. On the other hand, the consistency between the inverted profiles with these alternative estimates supports the reliability of the SWM approach, as also demonstrated by the good match with the *in situ* observed ground motion amplification (Aimar *et al.* 2022).

6 CONCLUSIONS

The solution of the inverse problem is a key step in surface wave analysis. The difficulties linked to the high non-linearity and the ill-posedness of the problem urge for the implementation of robust algorithms to return reliable earth models.

This paper proposed a novel algorithm for the joint estimate of *S*-wave velocity and damping ratio profiles from the experimental *R*-wave dispersion and attenuation parameters. The proposed scheme is a global search, Monte Carlo procedure that implements an optimized sampling procedure, based on the scaling properties of the Rayleigh eigenvalue problem in viscoelastic conditions. The validity of these scaling properties in the viscoelastic case has been demonstrated in this paper, and the effectiveness of the proposed inversion algorithm has been tested on two synthetic data sets. The Monte Carlo scheme allows for the investigation of a large population of candidate earth models, whereas the implementation of scaling properties concentrates the random samples in high probability density zones that are expected to be closer to the 'true' ground model. In this way, the number of random samples required to effectively investigate the parameter space can be reduced, thus saving computation time.

The effectiveness of the proposed algorithm was tested on the inversion of the experimental dispersion and attenuation data obtained from a MASW survey at the Garner Valley Downhole Array site. The improved sampling scheme resulted in well-constrained *S*-wave velocity and damping ratio profiles, especially in the near-surface layers. However, the estimated ground models are affected by large variability at depth, especially in terms of the *S*-wave damping ratio. The scatter is the combined effect of the high variability in low-frequency experimental data and the moderately low sensitivity of theoretical attenuation curves to D_S at great depths (e.g. Verachtert 2018). Therefore, experimental data do not allow for an effective constraint on D_S in the deep portions of the earth models. However, this limitation can be solved by exploiting ambient vibration data to get attenuation estimates in the low-frequency range, thus allowing a more reliable estimation of D_S at depth. On the other hand, the considerations above on data variability rely on a fixed-number suite of best-fitting ground models, which is a simplified description of actual data uncertainties and inversion non-uniqueness. Indeed, currently there are no available methods for selecting a statistical collection of samples from the joint inversion of phase velocity and phase attenuation data. For this reason, further studies on this topic will address this issue, by generalizing available criteria developed in the dispersion analysis or introducing new schemes, that account for the multivariate nature of the joint inversion.

Finally, the reliability of the derived ground models was addressed, by assessing the compatibility with estimates from alternative procedures. The general agreement with laboratory-based values highlights the reliability of surface wave data. Besides, the larger values of D_S in the shallow portion of the ground is consistent with the near-surface variability demonstrated in other studies (e.g. Fathi *et al.* 2016), which is responsible of additional attenuation mechanisms other than intrinsic dissipation. In summary, using surface wave data returns comparable damping models in respect of the interpretation of borehole array data. On the other hand, MASW testing does not require the realization of instrumented boreholes and therefore is much more flexible for site investigation in engineering applications.

Further improvements in the reliability of ground models could be obtained by including higher modes in the solution of the inverse problem, which in principle is a straightforward extension of the proposed scheme.

SUPPORTING INFORMATION

Supplementary data are available at *GJI* online.

Please note: Oxford University Press is not responsible for the content or functionality of any supporting materials supplied by the authors. Any queries (other than missing material) should be directed to the corresponding author for the paper.

ACKNOWLEDGMENTS

The authors are grateful to Mauro Francavilla, who helped in processing data measured at the Garner Valley Downhole Array. The study has been partially supported by the ReLUIS 3 project, funded by the Italian Civil Protection Agency. Data at the Garner Valley Downhole Array were extracted from the NSF Project 'Collaborative Research: 3D Ambient Noise Tomography (3D ANT) for Natural Hazards Engineering' grant CMMI-1931162. However, any

opinions, findings and conclusions or recommendations expressed in this material are those of the authors and do not necessarily reflect the views of the National Science Foundation. The seismic instruments were provided by the Incorporated Research Institutions for Seismology (IRIS) through the PASSCAL Instrument Center at New Mexico Tech. Data collected will be available through the IRIS Data Management Center. The facilities of the IRIS Consortium are supported by the National Science Foundation's Seismological Facilities for the Advancement of Geoscience (SAGE) Award under Cooperative Support Agreement EAR-1851048.

DATA AVAILABILITY

Synthetic waveform data and codes are available on request from the authors. Data at the Garner Valley Downhole Array were extracted from the NSF Project 'Collaborative Research: 3-D Ambient Noise Tomography (3D ANT) for Natural Hazards Engineering' grant CMMI-1931162, and they are available at http://service.iris.edu/ph5ws/.

REFERENCES

Achenbach, J.D. & Reddy, D.P., 1967. Note on wave propagation in linearly viscoelastic media, *Z. Angew. Math. Phys.,* **18,** 141–144.

Aimar, M., 2022. Uncertainties in the estimation of the shear-wave velocity and the small-strain damping ratio from surface wave analysis, *PhD thesis*, Politecnico di Torino, https://hdl.handle.net/11583/2972200.

Aimar, M., Foti, S. & Cox, B.R., 2024.Novel techniques for in-situ estimation of shear-wave velocity and damping ratio through MASW testing - I: A beamforming procedure for extracting Rayleigh-wave phase velocity and phase attenuation. *Geophys. J. Int.,* doi: 10.1093/gji/ggae051.

Aimar, M., Francavilla, M., Cox, B.R. & Foti, S., 2022. In-situ characterization of the near-surface small strain damping ratio at the Garner Valley downhole array through surface waves analysis, in *Proceedings of the 4th International Conference on Performance Based Design in Earthquake Geotechnical Engineering,* pp. 855–862, Springer International Publishing.

Aki, K. & Richards, P.G., 2002. *Quantitative Seismology,* University Science Books.

Armstrong, M.A., Ravasio, M., Versteijlen, W.G., Verschuur, D.J., Metrikine, A.V. & Van Dalen, K.N., 2020. Seismic inversion of soil damping and stiffness using multichannel analysis of surface wave measurements in the marine environment. *Geophys. J. Int.,* **221,** 1439–1449.

Badsar, S.A., 2012. In-Situ Determination of Material Damping in the Soil at Small Deformation Ratios (In situ bepaling van de materiaaldemping in de grond bij kleine vervormingen), *PhD thesis*, KU Leuven.

Bergamo, P., Maranò, S., Imperatori, W., Hobiger, M. & Fäh, D., 2019. Wavefield decomposition technique applied to active surface wave surveys: towards joint estimation of shear modulus and dissipative properties of the near-surface, in *EPOS@ SERA "Strong Motion Site Characterization" Workshop*.

Bonilla, L.F., Steidl, J.H., Gariel, J.C. & Archuleta, R.J., 2002. Borehole response studies at the Garner Valley downhole array, southern California. *Bull. seism. Soc. Am.,* **92,** 3165–3179.

Brown, L.T., Boore, D.M. & Stokoe, K.H., II, 2002. Comparison of shear-wave slowness profiles at 10 strong-motion sites from noninvasive SASW measurements and measurements made in boreholes. *Bull. seism. Soc. Am.,* **92,** 3116–3133.

Chandra, J., Guégen, P., Steidl, J.H. & Bonilla, L.F., 2015. In situ assessment of the G–γ curve for characterizing the nonlinear response of soil: application to the Garner Valley Downhole array and the Wildlife Liquefaction Array. *Bull. seism. Soc. Am.,* **105,** 993–1010.

Christensen, R., 2012. *Theory of Viscoelasticity: An Introduction,* Elsevier.

Comina, C., Foti, S., Boiero, D. & Socco, L.V., 2011. Reliability of VS,30 evaluation from surface-wave tests. *J. Geotech. Geoenv. Eng.,* **137,** 579–586.

Constable, S.C., Parker, R.L. & Constable, C.G., 1987. Occam's inversion: a practical algorithm for generating smooth models from electromagnetic sounding data. *Geophysics,* **52,** 289–300.

Coutant, O., 1996. Observation of shallow anisotropy on local earthquake records at the Garner Valley, Southern California, downhole array. *Bull. seism. Soc. Am.,* **86,** 477–488.

Cox, B. R. & Teague,, D., 2016. Layering ratios: a systematic approach to the inversion of surface wave data in the absence of a priori information. *Geophysical Journal International,* **207**(1), 422–438.

Cox, B.R., Wood, C.M. & Teague, D.P., 2014. Synthesis of the UTexas1 surface wave dataset blind-analysis study: inter-analyst dispersion and shear wave velocity uncertainty, in *Proceedings of the Geo-Congress 2014,* pp. 850–859, Atlanta.

Darendeli, M.B., 2001. Development of a new family of normalized modulus reduction and material damping curves, *PhD thesis*, University of Texas at Austin.

Fathi, A., Poursartip, B., Stokoe, K.H., II & Kallivokas, L.F., 2016. Three-dimensional P- and S-wave velocity profiling of geotechnical sites using full-waveform inversion driven by field data. *Soil Dyn. Earthq. Eng.,* **87,** 63–81.

Foti, S. & Strobbia, C., 2002. Some notes on model parameters for surface wave data inversion, in *Proceedings of the 15th EEGS Symposium on the Application of Geophysics to Engineering and Environmental Problems,* European Association of Geoscientists & Engineers.

Foti, S. *et al.* 2018. Guidelines for the good practice of surface wave analysis: a product of the InterPACIFIC project. *Bull. Earthq. Eng.,* **16,** 2367–2420.

Foti, S., 2000. Multistation methods for geotechnical characterization using surface waves, *PhD thesis*, Politecnico di Torino.

Foti, S., 2003. Small-strain stiffness and damping ratio of Pisa clay from surface wave tests. *Géotechnique,* **53,** 455–461.

Foti, S., Comina, C., Boiero, D. & Socco, L.V., 2009. Non-uniqueness in surface-wave inversion and consequences on seismic site response analyses. *Soil Dyn. Earth. Eng.,* **29,** 982–993.

Foti, S., Lai, C.G., Rix, G.J. & Strobbia, C., 2014. *Surface Wave Methods for Near-Surface Site Characterization,* CRC Press.

Gabriels, P., Snieder, R. & Nolet, G., 1987. In situ measurements of shear-wave velocity in sediments with higher-mode Rayleigh waves. *Geophys. Prospect.,* **35,** 187–196.

Garofalo, F. *et al.* 2016a. InterPACIFIC project: comparison of invasive and non-invasive methods for seismic site characterization. Part II: inter-comparison between surface-wave and borehole methods. *Soil Dyn. Earth. Eng.,* **82,** 241–254.

Garofalo, F. *et al.* 2016b. InterPACIFIC project: comparison of invasive and non-invasive methods for seismic site characterization. Part I: intra-comparison of surface wave methods. *Soil Dyn. Earth. Eng.,* **82,** 222–240.

Gibbs, J.F., 1989. Near-surface P- and S-wave velocities from bore hie measurements near Lake Hemet, California. *U.S. Dept. of the Interior, Geological Survey,* Open-File Report 89-630, U.S. Dept. of the Interior, Geological Survey, doi:10.3133/ofr89630.

Griffiths, S.C., Cox, B.R., Teague, D. & Rathje, E.M., 2016. Mapping dispersion misfit and uncertainty in Vs profiles to variability in site response estimates. *J. Geotech. Geoenv. Eng.,* **142,** 04016062.

Hallo, M., Imperatori, W., Panzera, F. & Fäh, D., 2021. Joint multizonal trans-dimensional Bayesian inversion of surface wave dispersion and ellipticity curves for local near-surface imaging. *Geophys. J. Int.,* **226,** 627–659.

Haskell, N.A., 1953. The dispersion of surface waves on multilayered media. *Bull. seism. Soc. Am.,* **43,** 17–34.

Herrmann, R.B. & Al-Eqabi, G.I., 1991. Surface wave inversion for shear wave velocity, in *Shear Waves in Marine Sediments,* Springer.

Hill, R.I., 1981. Geology of Garner Valley and vicinity, in *Geology of the San Jacinto Mountains, Annual Field Trip Guidebook No. 9,* eds Brown, A.R. & Ruff, R.W., South Coast Geological Society.

Lai, C.G. & Rix, G.J., 1998. Simultaneous inversion of Tayleigh phase velocity and attenuation for near-surface site characterization, *PhD thesis*, Georgia Institute of Technology.

Lai, C.G., Foti, S. & Rix, G.J., 2005. Propagation of data uncertainty in surface wave inversion. *J. Environ. Eng. Geophys.,* **10,** 219–228.

Lai, C.G., Rix, G.J., Foti, S. & Roma, V., 2002. Simultaneous measurement and inversion of surface wave dispersion and attenuation curves. *Soil Dynam. Earthq. Eng.,* **22,** 923–930.

Maraschini, M., Boiero, D., Foti, S. & Socco, L.V., 2011. Scale properties of the seismic wavefield perspectives for full-waveform matching. *Geophysics,* **76,** A37–A44.

Marosi, K.T. & Hiltunen, D.R., 2004. Characterization of SASW phase angle and phase velocity measurement uncertainty. *Geotech. Test. J.,* **27,** 205–213.

Martı´nez, M.D., Lana, X., Olarte, J., Badal, J. & Canas, J.A., 2000. Inversion of Rayleigh wave phase and group velocities by simulated annealing. *Phys. Earth planet. Inter.,* **122,** 3–17.

Misbah, A.S. & Strobbia, C., 2014. Joint estimation of modal attenuation and velocity from multichannel surface wave data. *Geophysics,* **79,** EN25–EN38.

Mosegaard, K. & Sambridge, M., 2002. Monte Carlo analysis of inverse problems. *Inverse Probl,* **18,** R29–R54.

Mosegaard, K. & Tarantola, A., 1995. Monte Carlo sampling of solutions to inverse problems. *J. geophys. Res.,* **100,** 12 431–12 447.

Nazarian, S. & Stokoe, K.H., II, 1984. Nondestructive testing of pavements using surface waves. *Transpl. Res. Rec.,* **993,** 67–79. https://onlinepubs.trb.org/Onlinepubs/trr/1984/993/993-009.pdf (last accessed December 2023).

O'Neill, A., 2004. Shear velocity model appraisal in shallow surface wave inversion, in *Proceedings of the Symposium on the Application of Geophysics to Engineering and Environmental Problems,* Society of Exploration Geophysicists.

Olafsdottir, E.A., Bessason, B. & Erlingsson, S., 2018. Combination of dispersion curves from MASW measurements. *Soil Dyn. Earthq. Eng.,* **113,** 473–487.

Oldenburg, D.W. & Li, Y., 2005. Inversion for applied geophysics: a tutorial, in *Near-Surface Geophysics,* ed. Butler, D.K., Society of Exploration Geophysicist.

Passeri, F., Comina, C., Foti, S. & Socco, L.V., 2021. The Polito Surface Wave flat-file Database (PSWD): statistical properties of test results and some inter-method comparisons. *Bull. Earthq. Eng.,* **19,** 2343–2370.

Passeri, F., Foti, S. & Rodriguez-Marek, A., 2020. A new geostatistical model for shear wave velocity profiles. *Soil Dyn. Earthq. Eng.,* **136,** 106247. doi: 10.1016/j.soildyn.2020.106247.

Rix, G.J., Lai, C.G. & Wesley Spang Jr., A., 2000. In situ measurement of damping ratio using surface waves. *J. Geotech. Geoenv. Eng.,* **126,** 472–480.

Schevenels, M., Degrande, G. & François, S., 2009. EDT: an elastodynamics toolbox for MATLAB. *Comput. Geosci.,* **35,** 1752–1754.

Seber, G.A.F. & Wild, C.J., 2003. *Nonlinear Regression,* John Wiley & Sons.

Sen, M.K. & Stoffa, P.L., 1996. Bayesian inference, Gibbs' sampler and uncertainty estimation in geophysical inversion. *Geophys. Prospect.,* **44,** 313–350.

Seylabi, E., Stuart, A.M. & Asimaki, D., 2020. Site characterization at downhole arrays by joint inversion of dispersion data and acceleration time series. *Bull. seism. Soc. Am.,* **110,** 1323–1337.

Shibuya, S., Mitachi, T., Fukuda, F. & Degoshi, T., 1995. Strain rate effects on shear modulus and damping of normally consolidated clay. *Geotech. Test. J.,* **18,** 365–375.

Shtivelman, V., 1999. Using surface waves for estimating shear wave velocities in the shallow subsurface onshore and offshore Israel, in *Proceedings of the 5th EEGS-ES Meeting,* European Association of Geoscientists & Engineers.

Socco, L.V. & Boiero, D., 2008. Improved Monte Carlo inversion of surface wave data. *Geophys. Prospect.,* **56,** 357–371.

Socco, L.V. & Strobbia, C., 2004. Surface-wave method for near-surface characterization: a tutorial. *Near Surf. Geophys.,* **2,** 165–185.

Spang, A.W., 1995. *In Situ Measurements of Damping Ratio Using Surface Waves,* Georgia Institute of Technology.

Steller, R., 1996. New borehole geophysical results at GVDA, NEES@UCSB Internal Report,. available at http://nees.ucsb.edu/sites/eot-dev.nees.ucsb.edu/files/facilities/docs/GVDA-Geotech-Stellar1996.pdf (last accessed January 2023).

Stokoe, K.H., II, Kurtulus, A. & Menq, F.-Y., 2004. *SASW Measurements at the NEES Garner Valley Test Site, California*. The University of Texas at Austin.

Strobbia, C., 2003. Surface wave methods. Acquisition, processing and inversion, *PhD thesis*, Politecnico di Torino.

Tao, Y. & Rathje, E.M., 2019. Insights into modelling small-strain site response derived from downhole array data. *J. Geotech. Geoenv. Eng.,* **145,** 04019023.

Tarantola, A. & Valette, B., 1982. Generalized nonlinear inverse problems solved using the least squares criterion. *Rev. Geophys.,* **20,** 219–232.

Tarantola, A., 2004. *Inverse Problem Theory and Methods for Model Estimation,* SIAM.

Teague, D., Cox, B.R., Bradley, B. & Wotherspoon, L., 2018a. Development of deep shear wave velocity profiles with estimates of uncertainty in the complex interbedded geology of Christchurch, New Zealand. *Earthq. Spectra,* **34,** 639–672.

Teague, D.P., Cox, B.R. & Rathje, E.M., 2018b. Measured vs. predicted site response at the garner valley downhole array considering shear wave velocity uncertainty from borehole and surface wave methods. *Soil Dyn. Earthq. Eng.,* **113,** 339–355.

Thomson, W.T., 1950. Transmission of elastic waves through a stratified solid medium. *Bull. seism. Soc. Am.,* **21,** 89–93.

Vantassel, J.P. & Cox, B.R., 2021a. A procedure for developing uncertainty-consistent Vs profiles from inversion of surface wave dispersion data. *Soil Dyn. Earthq. Eng.,* **145,** 106622.

Vantassel, J.P. & Cox, B.R., 2021b. SWinvert: a workflow for performing rigorous 1-D surface wave inversions. *Geophys. J. Int.,* **224,** 1141–1156.

Vantassel, J.P. & Cox, B.R., 2022. SWprocess: a workflow for developing robust estimates of surface wave dispersion uncertainty. *J. Seismol.,* **26,** 731–756.

Verachtert, R., 2018. Deterministic and probabilistic determination of dynamic soil characteristics, *PhD thesis*, KU Leuven.

Verachtert, R., Lombaert, G. & Degrande, G., 2017. Multimodal determination of Rayleigh dispersion and attenuation curves using the circle fit method. *Geophys. J. Int.,* **212,** 2143–2158.

Wathelet, M., Jongmans, D. & Ohrnberger, M., 2004. Surface-wave inversion using a direct search algorithm and its application to ambient vibration measurements. *Near Surf. Geophys.,* **2,** 211–221.

Wood, C.M. & Cox, B.R., 2012. A comparison of MASW dispersion uncertainty and bias for impact and harmonic sources, in *Proceedings of the GeoCongress 2012: State of the Art and Practice in Geotechnical Engineering,* pp. 2756–2765.

Xia, J., Miller, D.E. & Park, C.B., 1999. Estimation of near-surface shear-wave velocity by inversion of Rayleigh waves. *Geophysics,* **64,** 691–700.

Xia, J., Miller, R.D., Park, C.B. & Tian, G., 2002. Determining Q of near-surface materials from Rayleigh waves. *J. appl. Geophy.,* **51,** 121–129.

Xia, J., Xu, Y., Miller, R.D. & Ivanov, J., 2012. Estimation of near-surface quality factors by constrained inversion of Rayleigh-wave attenuation coefficients. *J. appl. Geophy.,* **82,** 137–144.